Chemical Science

ROYAL SOCIETY OF CHEMISTRY

EDGE ARTICLE

View Article Online
View Journal | View Issue

Cite this: *Chem. Sci.*, 2024, **15**, 11347

All publication charges for this article have been paid for by the Royal Society of Chemistry

Received 8th May 2024
Accepted 24th June 2024

DOI: 10.1039/d4sc03020f

rsc.li/chemical-science

Supramolecular engineering cascade regulates NIR-II J-aggregates to improve photodynamic therapy†

Huizhe Wang, Huijia Liu, Wenqing Li, Shuai Li, Jiaqi Zhang, Jingzhe Zang, Li Liu and Peng Wang *

Rational design of small organic molecule-based NIR-II photosensitizers (PSs) with high singlet oxygen quantum yield in aqueous solution for deep tissue imaging and cancer therapy still presents challenges. Herein, we devised a general synthesis strategy to obtain six NIR-II region PSs with tunable aggregation states by adjusting the steric effect, and all PSs possess longer NIR absorption/emission wavelengths with tails extending beyond 1200 nm. Notably, ATX-6 possessed a singlet oxygen quantum yield of 38.2% and exhibited concentration-dependent J-aggregation properties upon self-assembly in an aqueous solution. What's more, supramolecular engineering with DSPE-PEG_{2000} further enhanced its degree of J-aggregation, which was attributed to the dimer-excited reduction of the energy levels of the single-linear/triple-linear states and the facilitation of intersystem crossover processes. In addition, ATX-6 NPs showed superior photodynamic therapy effects and great potential in high-contrast *in vivo* bioimaging of the NIR-II region. These results provide valuable insights for achieving the diagnostic and therapeutic integration of tumors.

1. Introduction

A lack of patient compliance and high recurrence rates have severely limited the use of conventional treatment options such as chemotherapy, surgery, and radiotherapy. This has prompted continuous attempts to develop novel therapeutic strategies.[1–4] Photodynamic therapy (PDT) has gradually aroused the interest of researchers because of its advantages of non-invasiveness, high selectivity, larger depth of tumor penetration, absence of ionizing radiation, and fewer side effects.[5–8] Photosensitizers (PSs) including chloramphenicol e6, methylene blue, porphyrin, and protoporphyrin IX induce apoptosis in tumor cells by generating cytotoxic reactive oxygen species (ROS) under laser irradiation.[9–11] However, the strong absorption and scattering of light by biological tissues greatly weaken their therapeutic effect on deep tissues. The second near-infrared window (NIR-II; 1000–1700 nm) fluorescence emitters exhibited deeper tissue penetration, lower autofluorescence, and higher signal-to-noise ratio compared to the first region near-infrared ones (NIR-I; 650–900 nm).[12–16] Consequently, the development of photodynamic multifunctional agents featuring NIR-II fluorescence remains a challenging and highly promising task.

Organic molecules such as cyanine derivatives,[17] metal–organic complexes,[18] and aggregation-induced emission compounds are more biocompatible and biodegradable to inorganic nanomaterials including single-walled carbon nanotubes, semiconductor nanocrystals, and upconversion nanoparticles.[18–23] Nevertheless, poor aqueous solubility, weak photostability, limited targeting ability, and low fluorescence hinder their further clinical translation.[24–27] Fortunately, the development of organic nanoparticles enhanced drug bioavailability by adjusting their hydrophilicity and hydrophobicity. Additionally, the enhanced permeability and retention (EPR) effect allows agents to be passively delivered into tumors, enabling effective tumor diagnosis and treatment with low biotoxicity.[28,29] In aqueous solutions, organic molecules self-assemble into highly ordered face-to-face stacking arrangements of H-aggregates or slip-stacking arrangements of J-aggregates.[30–32] H-aggregates exhibit weak or non-luminous blue-shifted absorption, while J-aggregates have red-shifted absorption and emission wavelengths with higher extinction coefficients, making them promising candidates as efficient NIR-II emitters.[33–35] It is believed that H-aggregates enhance the photothermal effect by inhibiting fluorescence and intersystem crossover (ISC) processes while promoting non-radiative transition rates.[36] However J-aggregates improve the photodynamic effect by promoting intersystem crossover through a decrease in the energy gap (ΔE_{ST}) between the lowest excited single-linear state (S_1) and the lowest trilinear state (T_1).[37] However, currently reported NIR-II J-aggregates for PDT often exhibit

Department of Biomedical Engineering, School of Engineering, China Pharmaceutical University, Nanjing 210009, China. E-mail: wangpeng@cpu.edu.cn

† Electronic supplementary information (ESI) available. See DOI: https://doi.org/10.1039/d4sc03020f

unsatisfactory single-linear oxygen ($^1O_2$) quantum yield (Φ_Δ) and fluorescence quantum yields (Φ_F), which limits their diagnostic and therapeutic effects.[38–40] Therefore, it is urgent to design novel J-type emitters with tunable properties for NIR-II fluorescence imaging and PDT.

Only a few types of fluorophores with J-aggregation stacking properties have been reported, such as boron dipyrrolidine (BODIPY), cyanine-based PSs, and aggregation-induced emission compounds.[41,42] Unfortunately, the practical application of J-aggregates in the NIR-II region for PDT has faced certain limitations. For example, cyanine-based PSs often have short triplet-state lifetimes and low $^1O_2$ quantum yields, which restrict the widespread use of J-aggregates.[43–45] Besides, PSs with J-aggregation properties typically have large structural systems and involve cumbersome synthesis steps.[46–49] Hence, it is essential to construct a simple and universal synthesis strategy to enrich PS species with NIR-II fluorescence guidance for PDT of tumors. Most organic molecules featuring NIR-II region emission have two symmetric chromophores, leading to a virtual delocalization of excitons through round trips, thereby reducing the internal transition rate as governed by the energy gap law.[50,51] Furthermore, it has been observed that NIR-II PSs with symmetric chromophores generally exhibit low $^1O_2$ quantum yields.[52–54] Recent research has shown the potential of asymmetric structures. For instance, Cao and his colleagues reported a near-infrared semi-cyanine photosensitizer BHcy with an asymmetric structure, exhibiting a higher single-linear oxygen quantum yield (Φ_Δ = 12.9%).[38] Other studies by Zhou and Liu have demonstrated the competitive photodynamic effects of asymmetric NIR-II PSs, suggesting that the asymmetric strategy is a promising approach for designing novel PSs with NIR-II emission.[55,56]

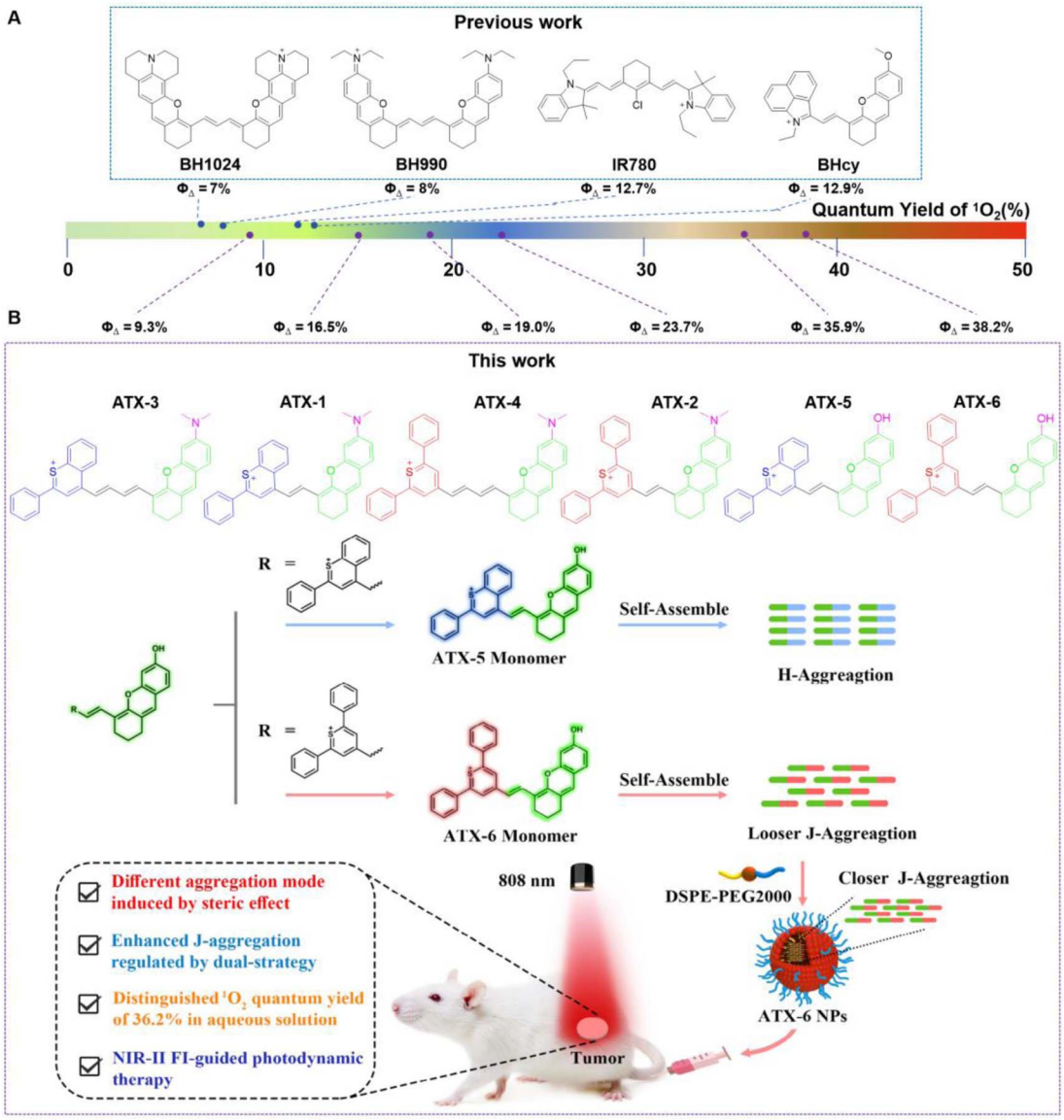

Fig. 1 (A) The reported photosensitizers with NIR-II region emission. (B) Rational design of NIR-II region photosensitizers in controllable aggregation mode.

Here, we designed a series of thiopyranonium–xanthene compounds ATX-1 to ATX-6, with asymmetric structures. The extended π-conjugated structures enable these compounds to absorb light in the range of 750 nm to 840 nm and emit light with primary wavelengths of 920 nm to 940 nm, with tails extending beyond 1200 nm. This significant extension improves the temporal and spatial resolution of NIR-II fluorescence imaging. Surprisingly, all the PSs demonstrate excellent $^1O_2$ quantum yield, with ATX-6 showing a particularly high yield ($\Phi_\Delta = 38.2\%$). In addition, ATX-5 also exhibits a high $^1O_2$ quantum yield ($\Phi_\Delta = 35.9\%$) and self-assembles into H-aggregates with blue-shifted absorption in water. Moreover, to further enhance its bioavailability, we encapsulated it into nanoparticles using DSPE-PEG_{2000}, but lower $^1O_2$ quantum yields were observed in both the H-aggregates and ATX-5 NPs. In contrast, ATX-6 self-assembles into J-aggregates with red-shifted absorption in water, resulting in a slightly reduced $^1O_2$ quantum yield. Notably, ATX-6 NPs encapsulated by DSPE-PEG_{2000} exhibit a similar $^1O_2$ quantum yield to the monomers. We hypothesized that self-assembled ATX-6 exhibited a loose J-aggregation state in aqueous solution, and after DSPE wrapping, the degree of J-aggregation was enhanced, leading to the increase of $^1O_2$ quantum yield (Fig. 1). On the other hand, the disparity in properties between ATX-5 and ATX-6 may be related to planarity. The optimized structures indicate that ATX-5, with benzopyranium heterocyclic substituents, occupies a larger spatial site resistance than ATX-6 with diphenylpyranium, and is less planar. Conversely, the lower planarity of the π-conjugated framework of ATX-6 facilitates the contact of the photosensitizer with the nearby substrate, thereby increasing the intramolecular charge transfer rate of the molecule, resulting in superior $^1O_2$ generation. Furthermore, ATX-5 possesses a hydrophobic portion with a dihedral angle of 68°, promoting the hydrophobic portion to be exposed. This exposure facilitates intermolecular hydrophobic interactions and the formation of hydrogen bonds, favoring the formation of H-aggregates. The dihedral angle of ATX-6 is extremely small, presenting a nearly planar structure, which makes the intermolecular interactions closer and promotes π–π stacking and J aggregation.

2. Results and discussion

2.1 Design and synthesis

Benzothiopyranium heterocycles and diphenylthiopyranium heterocycles with symmetrical structures have been applied in the design of PSs, but their poor $^1O_2$ yield limits them for further research into cancer treatment. The production of $^1O_2$ occurs through the light-induced transfer of electrons from a triplet-excited state of a PS to O_2. Therefore, PSs need to have an active and highly reactive triplet excited state for effective PDT function. We condensed a xanthene planar molecule with classic NIR-II emission with the methyl group of the pyranium heterocycle. This novel approach formed a planar and larger π conjugated structure of ATX PSs (Scheme S1†). This new structure may reduce the energy gap of ΔE_{ST}, promote the ISC process, and increase the quantum yield of $^1O_2$. The molecular structures of ATX PSs were analyzed and characterized using a Bruker spectrometer (Germany) and high-resolution mass spectrometry (HRMS), and data on the characterization and experimental procedures are provided in the ESI.†

2.2 Photophysical property study

The spectral properties of ATX PSs were first investigated in the monodisperse state. The absorption and emission spectra of ATX-1, ATX-2, ATX-3, and ATX-4 with nitrogen dimethyl substitution in dichloromethane (DCM) exhibited peaks at 825/930 nm, 837/933, 820/933 nm, and 841/939 nm respectively. On the other hand, ATX-5 and ATX-6 with hydroxyl substitution in DCM showed absorption wavelengths 790 nm and 757 nm, and both revealed a maximum near-infrared fluorescence emission peak at 923 nm (Fig. S1†). Most PSs exhibited a stokes shift of more than 100 nm which benefits from the strong D–A interaction and large π conjugated structure. Additionally, the excellent electron-donating energy of nitrogen dimethyl promoted intramolecular charge transfer (ICT) and further extended the absorption wavelength of the PSs.[57,58] Furthermore, all ATX PSs had better fluorescence quantum yield, particularly ATX-2 ($\Phi_F = 1.21\%$) and ATX-4 ($\Phi_F = 1.84\%$), which exhibited around 24 and 36-fold increased brightness compared to IR-26 ($\Phi_F = 0.05\%$). ATX-1, ATX-3 and ATX-5 have large dihedral angles, while ATX-2, ATX-4 and ATX-6 have nearly planar structures. Previous studies have shown that compounds with large dihedral angles are prone to twisting, and have large non-radiative decay rate constants, resulting in low photoluminescence quantum yields. The immobilization of the dimethylamino plane further inhibits the Twisted Intramolecular Charge Transfer (TICT) process, thus ATX-2 and ATX-4 have the highest photoluminescence quantum yields.[59]

To further investigate their photodynamic properties, DPBF was utilized to evaluate the $^1O_2$ quantum yield of the ATX PSs. Following 10 minutes of 808 nm laser irradiation, the absorption of other ATX PSs at 415 nm decreased significantly (ATX-1, $\Phi_\Delta = 16.5\%$; ATX-2, $\Phi_\Delta = 23.7\%$; ATX-3, $\Phi_\Delta = 9.3\%$; ATX-4, $\Phi_\Delta = 19.0\%$) (Table S1†). To our delight, ATX-5 and ATX-6 exhibited distinguished $^1O_2$ quantum yield (ATX-5, $\Phi_\Delta = 35.9\%$; ATX-6, $\Phi_\Delta = 38.2\%$) when compared to ICG ($\Phi_\Delta = 0.2\%$) and IR-1061 ($\Phi_\Delta = 7\%$), signifying them as suitable candidates for photodynamic therapy (Fig. S2†). The reason for the lower $^1O_2$ quantum yield of benzothiopyranonium xanthene PSs than diphenylthiopyranonium xanthene ones is the steric effect.

2.3 Spectral property research of aggregates and nanoparticles

After self-assembly in water, ATX-5 and ATX-6 aggregates exhibited lower stability and $^1O_2$ quantum yields than their corresponding monomers (ATX-5 aggregates, $\Phi_\Delta = 3.48\%$; ATX-6 aggregates, $\Phi_\Delta = 24.9\%$). Hence, we formulated ATX-5 NPs and ATX-6 NPs to enhance their optical properties for *in vitro* and *in vivo* biocompatibility by co-assembling DSPE-PEG_{2000} with the self-assembled aggregates (ATX-5 NPs, $\Phi_\Delta = 16.0\%$; ATX-6 NPs, $\Phi_\Delta = 30.9\%$). The concentration of the nanoparticles was determined from the UV absorption standard curve of the respective monomers in aqueous solution

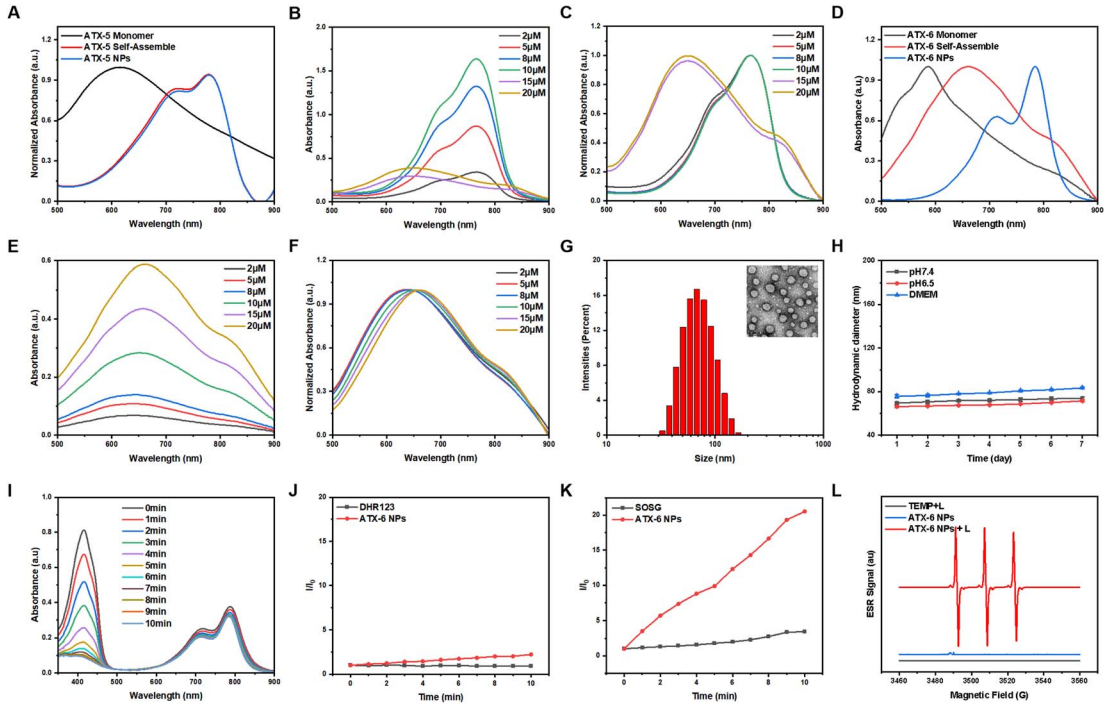

Fig. 2 (A) Absorption spectra of the ATX-5 monomer and different aggregates in aqueous solution. Concentration-dependent (B) normalized absorbance and (C) normalized fluorescence intensity of ATX-5 NPs. (D) Absorption spectra of the ATX-6 monomer and different aggregates in aqueous solution. Concentration-dependent (E) normalized absorbance and (F) normalized fluorescence intensity of ATX-6 NPs. (G) DLS size distribution of ATX-6 NPs in water. Inset: TEM image of ATX-6 NPs, scale bar = 100 nm. (H) Stabilities of ATX-6 NPs in different pH values of PBS or DMEM (containing 10% FBS) for 7 days. (I) $^1O_2$ generation of ATX-6 NPs (20 μM) at the pH value of 7.4 using DPBF as the probe. (J) PL intensity of DHR 123 (for $O_2^{\bullet-}$ detection) in the presence of ATX-6 NPs (20 μM) upon irradiation (808 nm, 1.5 W cm^{-2}) for different times. (K) Comparison of the PL intensity (I/I_0) of SOSG for $^1O_2$ detection after 808 nm laser irradiation. (L) ESR spectra to detect $^1O_2$ generated by ATX-6 NPs under illumination, using TEMP as a spin trap agent.

(Fig. S3†). To further elucidate the difference between the monomers, aggregates, and nanoparticles, we tested the UV absorption spectra of ATX-5 and ATX-6. The maximum absorption peaks of ATX-5 aggregates and ATX-5 NPs were very close, but both were red-shifted compared to their monomers (Fig. 2A). However, as the concentration of ATX-5 NPs increased, the UV absorption peak underwent a blue shift (Fig. 2B and C), which indicated H-aggregation.[60] The maximum absorption peaks of ATX-6 aggregates and ATX-6 NPs were also red-shifted compared to their monomers, and the red-shift range of ATX-6 NPs was larger than that of ATX-6 aggregates (Fig. 2D). We speculated that DSPE packaging has increased the degree of aggregation of the originally loose ATX-6 aggregates (Fig. 1B). In addition, the UV absorption peak of ATX-6 NPs also red-shifted with increasing concentration, which was consistent with the characteristic of J-aggregation (Fig. 2E and F). As ATX-6NPs had higher $^1O_2$ quantum yields and tunable aggregation properties, we utilized them in subsequent research.

ATX-6 NPs exhibited uniform diameters of ≈64 nm and spherical morphology based on dynamic light scattering (DLS) analysis and transmission electron microscopy (TEM) analysis (Fig. 2G). The stability of nanoparticles was evaluated for *in vivo* applications. Generally, ATX-6 NPs were dispersed in PBS with different pH values and DMEM medium containing 10% fetal bovine serum for 7 days, and the DLS results revealed that the changes of both nanoparticles were less than 10 nm (Fig. 2H), demonstrating their high physiological stability. Interestingly, ATX-6 NPs showed improved $^1O_2$ quantum yield at pH 6.5 (Φ_Δ = 34.3%) compared to pH 7.4 (Φ_Δ = 30.9%) due to the slightly acidic nature of the tumor microenvironment, which promotes J-aggregation (Fig. 2I and S4†). This result guides the use of ATX-6 NPs in the tumor microenvironment.

It is generally believed that when the lowest T_1 energy is higher than the oxygen sensitization threshold, PSs tend to rapidly generate $^1O_2$ through a type II process. The commercially available superoxide anion radical probe (DHR123) and $^1O_2$ fluorescence probe (SOSG) were further utilized to identify the species of ROS generated by ATX-6 NPs. Under 808 nm laser irradiation, no obvious enhancement of fluorescence intensity was observed with the DHR 123-only group and the ATX-6 NPs, reflecting their inferior $O_2^{\bullet-}$ production efficiency (Fig. 2J). However, the PL intensities of SOSG reached over 10.5-fold of the SOSG-only group in the presence of ATX-6 NPs under laser irradiation, suggesting high $^1O_2$ generation efficiency (Fig. 2K). As the most reliable technique in identifying short-lived ROS, electron paramagnetic resonance (EPR) spectroscopy was also applied to capture the ROS induced by ATX-6 NPs. In the presence of ATX-6 NPs and after 5 min of 808 nm laser irradiation, we observed apparent ESR signals originating from the

TEMP-$^1O_2$ adduct, while the EPR signal disappeared in the absence of illumination or NPs (Fig. 2L).

2.4 Theoretical calculation

Density functional theory (DFT) calculations were performed at the B3LYP/6-311G (d) level to explain the superior $^1O_2$ quantum yields of ATX PSs. The results showed an increasing positive potential from ATX-1 to ATX-4, with the strongest push–pull effect observed in ATX-4, validating the enhanced ICT effect (Fig. S5A and B†). The energy level of the lowest unoccupied molecular orbital (LUMO) decreased, and that of the highest occupied molecular orbital (HOMO) increased with an increase in polymethylene chains from ATX-1 to ATX-4. Additionally, ATX-3 and ATX-4 exhibited dispersed HOMO and LUMO distributions throughout the D–π–A skeleton, resulting in a significantly smaller HOMO–LUMO bandgap (E_g). This correlated well with the observed bathochromic shift in UV-vis-NIR spectroscopy (Fig. S5C†). On the other hand, undifferentiated electrostatic potentials and frontier molecular orbital density distributions were recorded for ATX-5 and ATX-6 (Fig. S6A–C†). In general, a larger dihedral angle leads to more exposure of the hydrophobic portion of the molecule, and hydrophobic interactions are one of the key drivers of H-aggregation. ATX-5 exhibits a highly distorted conformation with a torsion angle of 68° between the donor and acceptor units. This promotes hydrophobic interactions and hydrogen bond formation between molecules, which is more favorable for H-aggregation. When the molecule has a small dihedral angle, the conjugated structure within the molecule is more likely to remain planar, resulting in tighter interactions between molecules, which helps to promote π–π stacking and J-aggregation. The nearly planar structure of ATX-6 enhances the intermolecular π–π interactions in aqueous solution, which facilitates the transfer of energy and charge for the formation of J-aggregates (Fig. S6D†). Moreover, ATX-5 and ATX-6 shared higher T_1 energies than the threshold for oxygen sensitization (0.98 eV), verifying their potential as NIR-II photosensitizers (Table S2†).

To understand the mechanism of aggregation-induced enhancement of $^1O_2$ quantum yield, the electronic properties and properties of the ATX-5 dimer and ATX-6 dimer in the excited state were studied through theoretical calculations. The optimized geometries and frontier molecular orbitals were acquired *via* density functional theory (DFT) calculations at the B3LYP-D3BJ/6-311G* level (Fig. 3A). The HOMO and LUMO of ATX-5 dimers and ATX-6 dimers were delocalized in different molecules. This suggested that higher ICT exists in dimers. Moreover, ATX-5 dimers and ATX-6 dimers have lower energy gaps than their respective monomers. Besides, the lower energy gap confirmed that ATX-6 NPs were more easily excited by laser irradiation (Fig. 3B).

2.5 *In Vitro* phototherapeutic efficacy

The excellent *in vitro* photodynamic properties of ATX-6 NPs prompted us to explore their photocytotoxicity in cancer cells. Firstly, the cell viability assay was conducted in L02, MCF-7, and 4T1 cells using the CCK-8 assay. As depicted in Fig. 4A, ATX-6 NPs showed negligible cytotoxicity to normal cells at concentrations from 0 to 20 μM, suggesting low dark cytotoxicity. Unexpectedly, the dark toxicity of ATX-6 NPs to two breast cancer cells was more obvious, and the cell survival rate was below 80% at a concentration of 4 μM.

Upon 808 nm laser irradiation for 3 min, the cell viability of L02 decreased slightly with increasing concentration of ATX-6 NPs, and it was still higher than 80% at a concentration of 8 μM, further demonstrating that the toxicity to normal cells was negligible (Fig. S7A†). However, dose-dependent phototoxicity was observed for ATX-6 NP treated MCF-7 and 4T1 cells, leading to ≈95% and 80% cell deaths at a concentration of 8 μM (Fig. S7B and C†). The above results implied that ATX-6 NPs inherently possess tumor-suppressive effects. To verify this speculation, we tested the effect of ATX-6 on the activity of 4T1 cells. Due to the poor water solubility of ATX-6, most of it failed

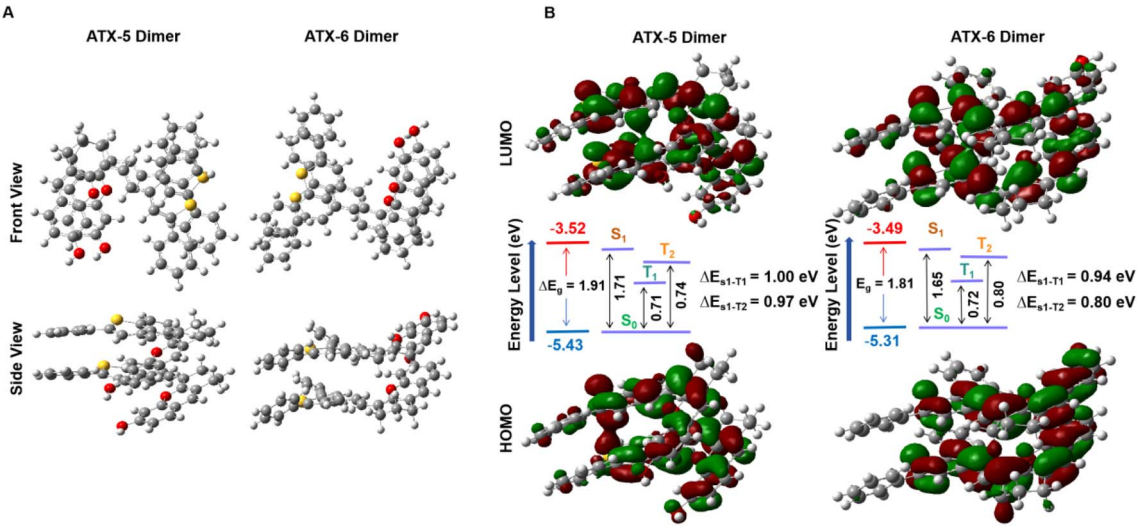

Fig. 3 (A) Optimized geometry of the ATX-5 dimers and ATX-6 dimers. (B) HOMO/LUMO of ATX-5 dimers and ATX-6 dimers in the ground state at the B3LYP/6-311G level.

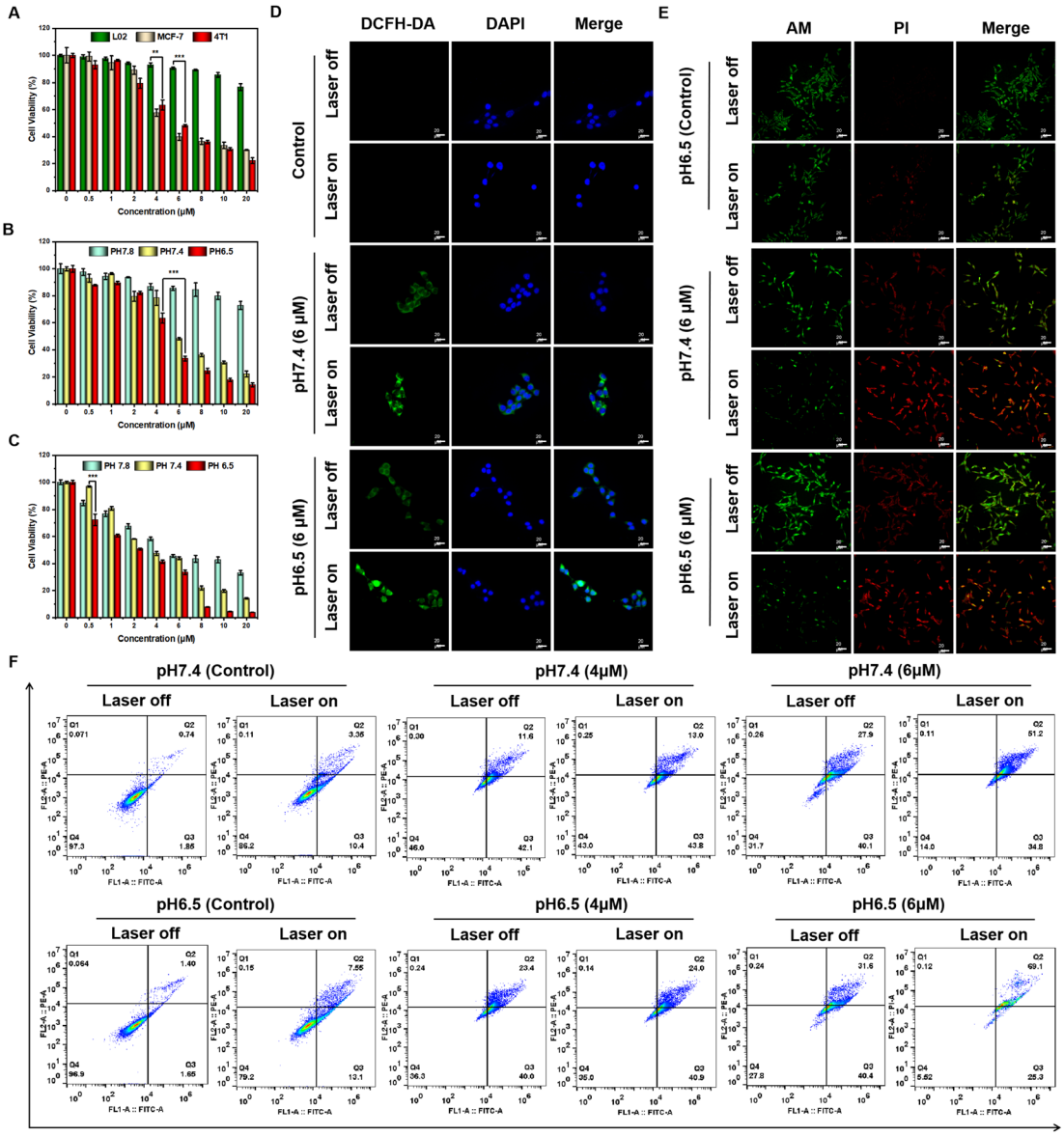

Fig. 4 (A) Cell viability of L02, MCF-7, and 4T1 cells incubated with ATX-6 NPs at varying concentrations without 808 nm laser irradiation. Viabilities of 4T1 cells treated with various concentrations of ATX-6 NPs (0–20 μM) at different pH values with (B) or without (C) 808 nm laser irradiation for 3 min (1.5 W cm^{-2}). The data are presented as mean ± SD ($n = 6$), *$P < 0.05$, **$P < 0.01$, ***$P < 0.001$, and ****$P < 0.0001$. (D) Detection of intracellular ROS generation by DCFH-DA in 4T1 cells after various treatments under pH 6.5 conditions with or without 808 nm laser irradiation (1.5 W cm^{-2}, 3 min). Scale bar: 20 μm. (E) Fluorescence images of calcein AM (green, live cells) and propidium iodide (red, dead cells) costained 4T1 cells treated with ATX-6 NPs at pH 6.5 with or without 808 nm laser irradiation (1.5 W cm^{-2}, 3 min) scale bar: 20 μm. (F) Flow cytometry with Annexin V-FITC and propidium iodide (PI) to evaluate the apoptosis and necrosis rates of ATX-6 NPs after different treatments.

to enter the cells, but it still manifested excellent tumor cytotoxicity at a concentration of 20 μM (Fig. S7D†). In addition, since ATX-6 NPs have better $^1O_2$ quantum yield at pH 6.5, we verified the effect of ATX-6 NPs on tumor cells under different pH conditions. As expected, ATX-6 NPs were able to induce maximum cell death under acidic conditions with 808 nm laser irradiation (Fig. 4B and C).

Since 2,7-dichlorofluorescein diacetate (DCFH-DA) can emit significant green fluorescence after oxidation by intracellular ROS, a commercial DCFH-DA probe was applied to measure the efficiency of intracellular ROS production by ATX-6 NPs at different pH values. As illustrated in Fig. 4D and S8,† ATX-6 NPs exhibited weak green fluorescence at pH 7.4 without laser irradiation, whereas dose-dependent enhanced fluorescence was detected when the laser was turned on. Besides, ATX-6 NPs at pH 6.5 showed the strongest green fluorescence, implying the higher production of $^1O_2$ inside the cells (Fig. S9†). This was further confirmed by live/dead cell staining experiments; strong red fluorescence was imaged with 808 nm laser irradiation, while only weak red fluorescence appeared when the laser was off. What's more, a dose-dependent increase in red fluorescence was also captured and it resulted in maximal cell death at pH

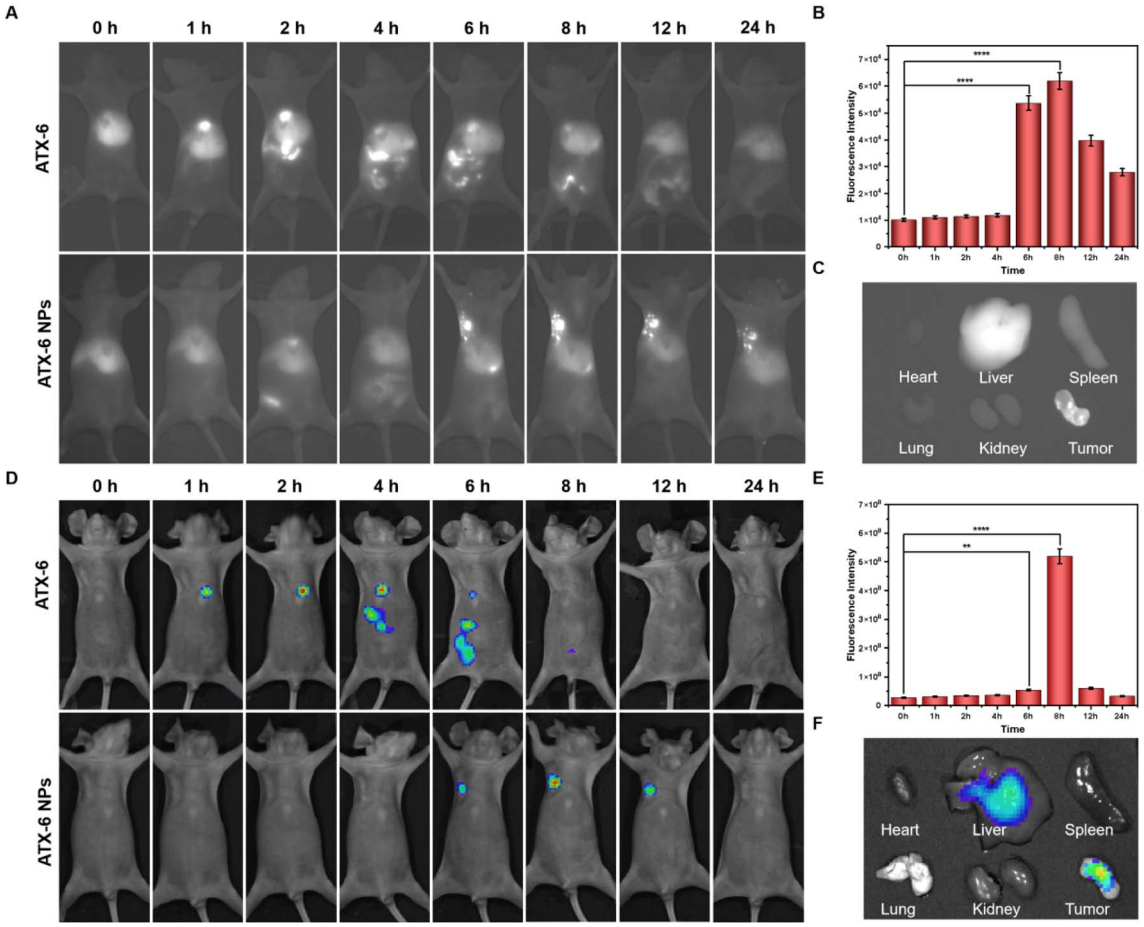

Fig. 5 (A) *In vivo* NIR-II fluorescence images (900 nm filter) of 4T1-tumor-bearing mice at different time points after intravenous injection of 100 μL ATX-6 or ATX-6 NPs (20 μM). (B) Quantification of fluorescence intensity of 4T1 tumor-bearing BALB/c mice using the NIR-II fluorescence imaging system (900 nm filter) at different time points after intravenous injection of ATX-6 NPs. (C) The bio-distribution of ATX-6 NPs in the tumor, heart, liver, spleen, lung, and kidney 24 h after intravenous injection with the NIR-II fluorescence imaging system (900 nm filter). (D) *In vivo* NIR-I fluorescence imaging of 4T1 tumor-bearing living mice at different time points after intravenous injection of 100 μL of ATX-6 or ATX-6 NPs (20 μM). (E) Quantification of fluorescence intensity of 4T1 tumor-bearing BALB/c mice using the NIR-I fluorescence imaging system at different time points after intravenous injection of ATX-6 NPs. (F) The bio-distribution of ATX-6 NPs in the tumor, heart, liver, spleen, lung, and kidney 24 h after intravenous injection with the NIR-I fluorescence imaging system. Data are means ± SD. *P < 0.05, **P < 0.01, ***P < 0.001, and ****P < 0.0001.

6.5 (Fig. 4E and S10†). All these results demonstrated that ATX-6 NPs exert enhanced tumor killing under acidic conditions.

Subsequently, Annexin V-FITC and PI commercial kits were used to further quantify the proportion of apoptotic cells by flow cytometry. As shown in Fig. 4F, the apoptosis ratio presented a significant positive correlation with incubation concentration. And ATX-6 NPs with 808 nm laser irradiation induced higher 4T1 cell late apoptosis at pH 6.5 (69.1%) compared with that at pH 7.4 (51.2%). Scratch assays were performed to evaluate ATX-6 NPs in tumor cell migration and invasion inhibition. After incubation with ATX-6 NPs dispersed in a culture medium of different pH for different times, the 4T1 cells' gap was significantly larger than that of the control group and in a concentration-dependent manner (Fig. S11 and S12†). Upon laser irradiation, there was almost no reduction in cell spacing in the ATX-6 NP treated cells, which indicated that ATX-6 NPs under laser exposure could effectively inhibit cell proliferation and migration (Fig. S13†).

2.6 *In Vivo* NIR-II and NIR-I FL imaging

Before conducting animal experiments, the *in vivo* cytotoxicity was characterized according to a standard hemolytic analysis (Fig. S14 and Table S3†). No hemolysis was observed in fresh rat blood treated with ATX-6 or ATX-6 NPs, and the hemolysis percentages in both groups were maintained lower than 2%, indicating their good hemocompatibility. Next, we studied the tumor accumulation and biodistribution of ATX-6 and ATX-6 NPs in 4T1 tumor-bearing BALB/c mice *via* intravenous injection. The NIR-II fluorescence of ATX-6 NPs in tumors increased over time and reached the maximum at 8 h post-injection (Fig. 5A and B, S15†). In addition, we quantified the signal-to-background ratio (SBR) values of ATX-6 NPS at different times. As shown in Fig. S16,† ATX-6 NPs showed a significant SBR value 6 h after injection (P < 0.0001). To examine the bio-distribution and metabolism of ATX-6 NPs, we euthanized treated mice 24 hours after injection and removed their major

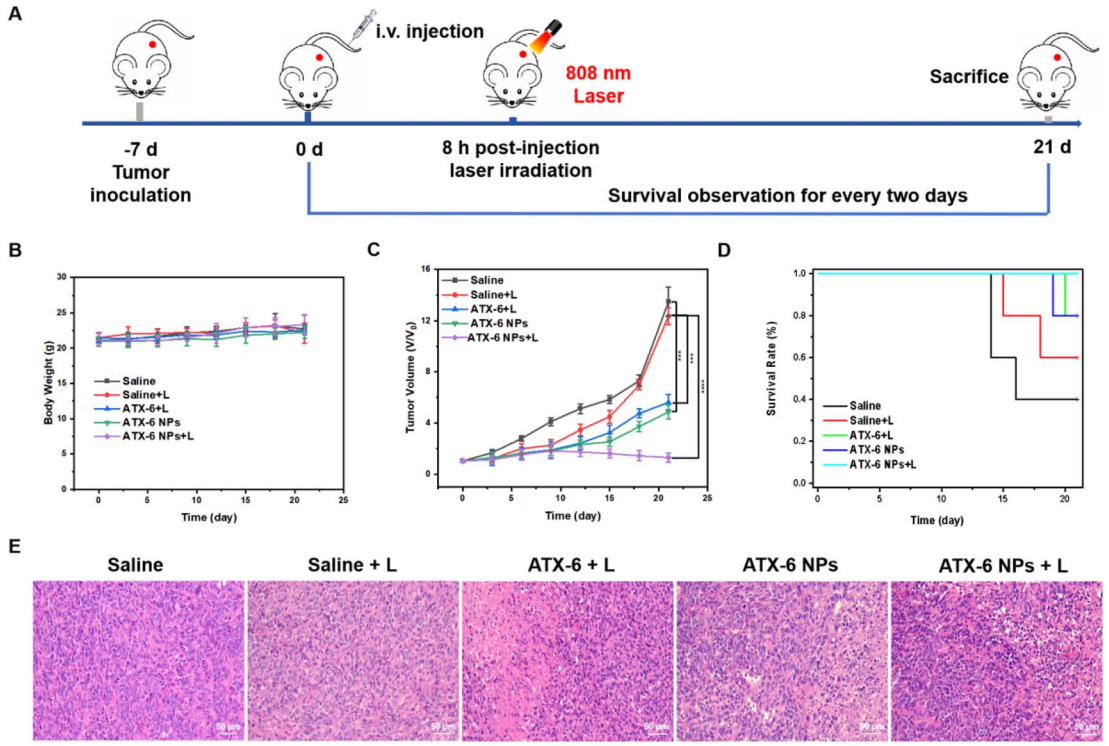

Fig. 6 (A) Schematic illustration of the experiment design to evaluate photodynamic therapy of ATX-6 NPs. (B) Body weight changes, (C) tumor volume growth curve, and (D) survival plot of 4T1 tumor-bearing mice treated with different preparations. Data are means ± SD. *P < 0.05, **P < 0.01, ***P < 0.001, and ****P < 0.0001. (E) H&E staining of tumor tissues from mice at 21 days after various treatments. Scale bar: 100 μm.

organs and tumor tissues for *ex vivo* imaging using NIR fluorescence. Mouse tumors accumulated the most NIR-II fluorescence, while the liver played a significant role in eliminating NPs from the body through hepatic metabolism (Fig. 5C, S17, and S18†). In contrast, ATX-6 was located in the liver dominantly, and it was fully metabolized after about 8 h-administration (Fig. S19 and S20†). The representative *ex vivo* tumor images further demonstrated efficient tumor-specific uptake and retention of ATX-6 NPs. These overall results indicated that ATX-6 NPs can effectively accumulate in tumors and support NIR-II fluorescence imaging-guided PDT. Likewise, the same results as above were obtained in the live imaging system in the NIR I region (Fig. 5D–F, and S21†).

2.7 NIR-II guided photodynamic therapy *in vivo*

Briefly, 4T1 tumor-bearing mice with a tumor volume of ≈50 mm^3 received various treatments. 8 h post-injection, the illuminated group was subjected to 5 minutes of laser irradiation (808 nm, 1.5 W cm^{-2}). During the 21 days of treatment, the volumes of tumors and the body weight of mice were monitored every two days (Fig. 6A). First, there was no significant change in the body weight over the 21-day treatment period (Fig. 6B), verifying the negligible toxicity of ATX-6 NPs to normal organs. As demonstrated in Fig. 6C and S22,† the mice injected with saline with or without the 808 nm laser irradiation showed rapid tumor growth, while for the ATX-6 + laser group and ATX-6 NP group, more pronounced tumor suppression effects were measured, but there appeared slight recurrence. Notably, the mice treated with ATX-6 NPs upon 808 nm laser irradiation achieved significant tumor elimination, but slightly burned scars on the tumor sites, and the scars healed gradually in a few days. All the mice treated with ATX-6 NPs upon 808 nm laser irradiation survived euthanasia, which also illustrated the excellent anti-tumor effect of ATX-6 NPs (Fig. 6D). To further confirm *in vivo* phototherapeutic efficacy, the excised tumor slices were examined using hematoxylin and eosin (H&E) staining analysis. As shown in Fig. 6E, ATX-6 NPs strongly caused apoptosis and necrosis in tumor tissues when exposed to NIR radiation. Additionally, there was no substantial damage or distinct inflammation lesions in the main organs, including the heart, liver, spleen, lung, and kidney (Fig. S23†), revealing the good biocompatibility of ATX-6 NPs and nontoxicity of the therapeutic process to mice.

To estimate the biosafety of ATX-6 NPs for further applications, hematological index, and blood biochemical parameters were assessed 7 days after injection of saline, ATX-6, and ATX-6 NPs. As shown in Fig. S24,† hemoglobin, and the number of white blood cells, lymphocytes and neutrophils, were all unaltered according to the routine blood testing. Similarly, there was no discernible difference between the experimental and control groups (saline) when liver function tests were performed. The values were generally within the range of the references, indicating that the treated mice had normal liver and kidney function (Fig. S25†). In summary, these results further demonstrated the safety and tolerable toxicity of ATX-6 NPs.

3. Conclusion

We have designed a series of asymmetric thiopyranonium-xanthene-based photosensitizers. Due to steric effects, the diphenyl heterocyclic substitutions showed superior single-linear oxygen quantum yields to the benzene heterocyclic substitutions, and ATX-5 and ATX-6 exhibited $^1O_2$ quantum yields as high as 35.9% and 38.2% in aqueous solution. The large π-conjugated structure allowed ATX-5 to self-assemble into concentration-dependent H-aggregates, while ATX-6 exhibited concentration-dependent J-aggregation properties. In addition, the amphiphilic DSPE-PEG_{2000} encapsulation of ATX-6 caused the originally loose J-aggregation to become more tightly packed, leading to an increase in the $^1O_2$ quantum yield. On the other hand, ATX-5 did not change its properties much after encapsulation, whereas the lower planar framework of ATX-6 facilitates the contact of the photosensitizer with the nearby substrate thereby increasing the rate of electromolecular intramolecular charge transfer, resulting in superior $^1O_2$ generation. The smaller HOMO–LUMO bandgap and lower energy gap between the lowest excited singlet state (S_1) and triplet state of T_1 also supported the above results. Moreover, the biocompatible ATX-6 NPs exhibited excellent NIR-II fluorescence-guided photodynamic therapy both *in vitro* and *in vivo*. This contribution provides a novel design strategy for tunable phototherapeutic agents, which is important for photodynamic therapy to enter clinical trials.

Data availability

The data that support the findings of this study are available from the corresponding author upon reasonable request.

Author contributions

H. Wang: conceptualization, methodology, investigation, data analysis, visualization, writing – original draft preparation, writing – reviewing and editing; H. Liu: methodology, investigation, data analysis, manuscript drafting; W. Li: methodology, investigation, data analysis, manuscript drafting; S. Li: visualization, data analysis, manuscript drafting; J. Zhang: visualization, writing – original draft preparation; J. Zang: visualization, data analysis, manuscript drafting; L. Liu: visualization, data analysis, manuscript drafting; P. Wang: conceptualization, funding acquisition, supervision, data analysis, manuscript drafting, writing – reviewing and editing.

Conflicts of interest

There are no conflicts to declare.

Acknowledgements

We acknowledge funding support from the National Natural Science Foundation of China (NSFC 82071979). Meanwhile, the authors thank Jiangsu Southeast Nanomaterials Co. Ltd for providing DSPE-PEG_{2000}.

References

1 Z. Xu, Y. Jiang, M. Fan, S. Tang, M. Liu, W. C. Law, C. Yang, M. Ying, M. Ma, B. Dong, K. T. Yong and G. Xu, Aggregation-Induced Emission Nanoprobes Working in the NIR-II Region: From Material Design to Fluorescence Imaging and Phototherapy, *Adv. Opt. Mater.*, 2021, **9**, 2100859.
2 H. Xiao, G. l. Wu, S. Tan, X. Tan and Q. Yang, Recent Progress on Tumor Microenvironment-Activated NIR-II Phototheranostic Agents with Simultaneous Activation for Diagnosis and Treatment, *Chem.–Asian J.*, 2024, e202301036.
3 Z. Tang, Y. Liu, M. He and W. Bu, Chemodynamic Therapy: Tumour Microenvironment-Mediated Fenton and Fenton-like Reactions, *Angew. Chem., Int. Ed.*, 2019, **58**, 946.
4 H. Sung, J. Ferlay, R. L. Siegel, M. Laversanne, I. Soerjomataram, A. Jemal and F. Bray, Global Cancer Statistics 2020: GLOBOCAN Estimates of Incidence and Mortality Worldwide for 36 Cancers in 185 Countries, *Ca-Cancer J. Clin.*, 2021, **71**, 209–249.
5 Y. Wang, L. Feng and S. Wang, Conjugated Polymer Nanoparticles for Imaging, Cell Activity Regulation, and Therapy, *Adv. Funct. Mater.*, 2019, **29**, 1806818.
6 K. Wen, H. Tan, Q. Peng, H. Chen, H. Ma, L. Wang, A. Peng, Q. Shi, X. Cai and H. Huang, Achieving Efficient NIR-II Type-I Photosensitizers for Photodynamic/Photothermal Therapy upon Regulating Chalcogen Elements, *Adv. Mater.*, 2022, **34**, 2108146.
7 Q. Lv, X. Yang, M. Wang, J. Yang, Z. Qin, Q. Kan, H. Zhang, Y. Wang, D. Wang and Z. He, Mitochondria-targeted prostate cancer therapy using a near-infrared fluorescence dye-monoamine oxidase A inhibitor conjugate, *J. Controlled Release*, 2018, **279**, 234–242.
8 H. Zhao, K. Chen, M. Liu, Z. Wang, L. Li, M. Li, P. Sun, H. Zhou, Q. Fan and Q. Shen, A Mitochondria-Targeted NIR-II Molecule Fluorophore for Precise Cancer Phototheranostics, *J. Med. Chem.*, 2024, **67**, 467–478.
9 X. Li, J. F. Lovell, J. Yoon and X. Chen, Clinical development and potential of photothermal and photodynamic therapies for cancer, *Nat. Rev. Clin. Oncol.*, 2020, **17**, 657.
10 P. Agostinis, K. Berg, K. A. Cengel, T. H. Foster, A. W. Girotti, S. O. Gollnick, S. M. Hahn, M. R. Hamblin, A. Juzeniene, D. Kessel, M. Korbelik, J. Moan, P. Mroz, D. Nowis, J. Piette, B. C. Wilson and J. Golab, Photodynamic therapy of cancer: An update, *Ca-Cancer J. Clin.*, 2011, **61**, 250.
11 W. Cao, Y. Zhu, F. Wu, Y. Tian, Z. Chen, W. Xu, S. Liu, T. Liu and H. Xiong, Three Birds with One Stone: Acceptor Engineering of Hemicyanine Dye with NIR-II Emission for Synergistic Photodynamic and Photothermal Anticancer Therapy, *Small*, 2022, **18**, 2204851.
12 H. Wan, H. Du, F. Wang and H. Dai, Molecular Imaging in the Second Near-Infrared Window, *Adv. Funct. Mater.*, 2019, **29**, 1900566.
13 C. Xu and K. Pu, Second near-infrared photothermal materials for combinational nanotheranostics, *Chem. Soc. Rev.*, 2021, **50**, 1111.

14 C. Li, G. Chen, Y. Zhang, F. Wu and Q. Wang, Advanced Fluorescence Imaging Technology in the Near-Infrared-II Window for Biomedical Applications, *J. Am. Chem. Soc.*, 2020, **142**, 14789.
15 W. Huang, H. Yang, Z. Hu, Y. Fan, X. Guan, W. Feng, Z. Liu and Y. Sun, Rigidity Bridging Flexibility to Harmonize Three Excited-State Deactivation Pathways for NIR-II-Fluorescent-Imaging-Guided Phototherapy, *Adv. Healthcare Mater.*, 2021, **10**, 2101003.
16 Y. Zheng, Q. Li, J. Wu, Z. Luo, W. Zhou, A. Li, Y. Chen, T. Rouzi, T. Tian, H. Zhou, X. Zeng, Y. Li, X. Cheng, Y. Wei, Z. Deng, F. Zhou and X. Hong, All-in-one mitochondria-targeted NIR-II fluorophores for cancer therapy and imaging, *Chem. Sci.*, 2021, **12**, 1843.
17 S. Liu, H. Ou, Y. Li, H. Zhang, J. Liu, X. Lu, R. T. K. Kwok, J. W. Y. Lam, D. Ding and B. Z. Tang, Planar and Twisted Molecular Structure Leads to the High Brightness of Semiconducting Polymer Nanoparticles for NIR-IIa Fluorescence Imaging, *J. Am. Chem. Soc.*, 2020, **142**, 15146.
18 M. Li, Z. Lu, J. Zhang, L. Chen, X. Tang, Q. Jiang, Q. Hu, L. Li, J. Liu and W. Huang, Near-Infrared-II Fluorophore with Inverted Dependence of Fluorescence Quantum Yield on Polarity as Potent Phototheranostics for Fluorescence-Image-Guided Phototherapy of Tumors, *Adv. Mater.*, 2023, **35**, 2209647.
19 S. Wang, Y. Fan, D. Li, C. Sun, Z. Lei, L. Lu, T. Wang and F. Zhang, Anti-quenching NIR-II molecular fluorophores for *in vivo* high-contrast imaging and pH sensing, *Nat. Commun.*, 2019, **10**, 1058.
20 X. Cai, A. Bandla, D. Mao, G. Feng, W. Qin, L. D. Liao, N. Thakor, B. Z. Tang and B. Liu, Biocompatible Red Fluorescent Organic Nanoparticles with Tunable Size and Aggregation-Induced Emission for Evaluation of Blood–Brain Barrier Damage, *Adv. Mater.*, 2016, **28**, 8760.
21 S. Ling, X. Yang, C. Li, Y. Zhang, H. Yang, G. Chen and Q. Wang, Tumor Microenvironment-Activated NIR-II Nanotheranostic System for Precise Diagnosis and Treatment of Peritoneal Metastasis, *Angew. Chem., Int. Ed.*, 2020, **59**, 7219.
22 J. Xu, R. Shi, G. Chen, S. Dong, P. Yang, Z. Zhang, N. Niu, S. Gai, F. He, Y. Fu and J. Lin, All-in-One Theranostic Nanomedicine with Ultrabright Second Near-Infrared Emission for Tumor-Modulated Bioimaging and Chemodynamic/Photodynamic Therapy, *ACS Nano*, 2020, **14**, 9613.
23 D. Yao, Y. Wang, R. Zou, K. Bian, P. Liu, S. Shen, W. Yang, B. Zhang and D. Wang, Molecular Engineered Squaraine Nanoprobe for NIR-II/Photoacoustic Imaging and Photothermal Therapy of Metastatic Breast Cancer, *ACS Appl. Mater. Interfaces*, 2020, **12**, 4276.
24 S. Wang, J. Liu, C. C. Goh, L. G. Ng and B. Liu, NIR-II-Excited Intravital Two-Photon Microscopy Distinguishes Deep Cerebral and Tumor Vasculatures with an Ultrabright NIR-I AIE Luminogen, *Adv. Mater.*, 2019, **31**, 1904447.
25 C. Liu, S. Zhang, J. Li, J. Wei, K. Müllen and M. Yin, A Water-Soluble, NIR-Absorbing Quaterrylenediimide Chromophore for Photoacoustic Imaging and Efficient Photothermal Cancer Therapy, *Angew. Chem.*, 2019, **131**, 1652.
26 J. Du, S. Liu, P. Zhang, H. Liu, Y. Li, W. He, C. Li, J. H. C. Chau, R. T. K. Kwok, J. W. Y. Lam, L. Cai, Y. Huang, W. Zhang, J. Hou and B. Z. Tang, Highly Stable and Bright NIR-II AIE Dots for Intraoperative Identification of Ureter, *ACS Appl. Mater. Interfaces*, 2020, **12**, 8040.
27 Z. Lei and F. Zhang, Molecular Engineering of NIR-II Fluorophores for Improved Biomedical Detection, *Angew. Chem., Int. Ed.*, 2021, **60**, 16294.
28 P. Liang, H. Tang, R. Gu, L. Xue, D. Chen, W. Wang, Z. Yang, W. Si and X. Dong, A pH-responsive zinc (II) metalated porphyrin for enhanced photodynamic/photothermal combined cancer therapy, *Sci. China Mater.*, 2019, **62**, 1199–1209.
29 Y. Cai, C. Tang, Z. Wei, C. Song, H. Zou, G. Zhang, J. Ran and W. Han, Fused-Ring Small-Molecule-Based Bathochromic Nano-agents for Tumor NIR-II Fluorescence Imaging-Guided Photothermal/Photodynamic Therapy, *ACS Appl. Bio Mater.*, 2021, **4**, 1942–1949.
30 H. Zhang, Z. Zhao, A. T. Turley, L. Wang, P. R. McGonigal, Y. Tu, Y. Li, Z. Wang, R. T. K. Kwok, J. W. Y. Lam and B. Z. Tang, Aggregate Science: From Structures to Properties, *Adv. Mater.*, 2020, **32**, 2001457.
31 X. Hu, C. Zhu, F. Sun, Z. Chen, J. Zou, X. Chen and Z. Yang, J-Aggregation Strategy toward Potentiated NIR-II Fluorescence Bioimaging of Molecular Fluorophores, *Adv. Mater.*, 2024, **36**, 2304848.
32 Y. Tian, D. Yin and L. Yan, J-aggregation strategy of organic dyes for near-infrared bioimaging and fluorescent image-guided phototherapy, *Wiley Interdiscip. Rev.: Nanomed. Nanobiotechnol.*, 2023, **15**, e1831.
33 S. Li, L. Fu, X. Xiao, H. Geng, Q. Liao, Y. Liao and H. Fu, Regulation of Thermally Activated Delayed Fluorescence to Room-Temperature Phosphorescent Emission Channels by Controlling the Excited-States Dynamics *via* J- and H-Aggregation, *Angew. Chem., Int. Ed.*, 2021, **60**, 18059.
34 K. Li, X. Duan, Z. Jiang, D. Ding, Y. Chen, G. Q. Zhang and Z. Liu, J-aggregates of meso-[2.2]paracyclophanyl-BODIPY dye for NIR-II imaging, *Nat. Commun.*, 2021, **12**, 2376.
35 Y. Tian, D. Yin, Q. Cheng, H. Dang, C. Teng and L. Yan, Supramolecular J-aggregates of aza-BODIPY by steric and π–π interactions for NIR-II phototheranostics, *J. Mater. Chem. B*, 2022, **10**, 1650–1662.
36 F. Wu, Y. Lu, X. Mu, Z. Chen, S. Liu, X. Zhou, S. Liu and Z. Li, Intriguing H-Aggregates of Heptamethine Cyanine for Imaging-Guided Photothermal Cancer Therapy, *ACS Appl. Mater. Interfaces*, 2020, **12**, 32388–32396.
37 Z. Li, P. Z. Liang, L. Xu, X. X. Zhang, K. Li, Q. Wu, X. F. Lou, T. B. Ren, L. Yuan and X. B. Zhang, *In situ* orderly self-assembly strategy affording NIR-II-J-aggregates for *in vivo* imaging and surgical navigation, *Nat. Commun.*, 2023, **14**, 1843.
38 W. Cao, Y. Zhu, F. Wu, Y. Tian, Z. Chen, W. Xu, S. Liu, T. Liu and H. Xiong, Three Birds with One Stone: Acceptor Engineering of Hemicyanine Dye with NIR-II Emission for

Synergistic Photodynamic and Photothermal Anticancer Therapy, *Small*, 2022, **18**, 2204851.

39 H. Bian, D. Ma, X. Zhang, K. Xin, Y. Yang, X. Peng and Y. Xiao, Tailored Engineering of Novel Xanthonium Polymethine Dyes for Synergetic PDT and PTT Triggered by 1064 nm Laser toward Deep-Seated Tumors, *Small*, 2021, **17**, 2100398.

40 H. Huang, D. Ma, Q. Liu, D. Huang, X. Zhao, Q. Yao, T. Xiong, S. Long, J. Du, J. Fan and X. J. Peng, Enhancing Intersystem Crossing by Intermolecular Dimer-Stacking of Cyanine as Photosensitizer for Cancer Therapy, *CCS Chem.*, 2022, **4**, 3627–3636.

41 Q. Xia, Y. Zhang, Y. Li, Y. Li, Y. Li, Z. Feng, X. Fan, J. Qian and H. Lin, A historical review of aggregation-induced emission from 2001 to 2020: A bibliometric analysis, *Aggregate*, 2022, **3**, e152.

42 J. Jia, Z. Ma, J. Zhuang, L. Huo, C. Zhou, N. Li and N. Zhao, Lipid droplet-targeted NIR AIE photosensitizer evoking concurrent ferroptosis and apoptosis, *Aggregate*, 2024, e516.

43 K. W. Lee, Y. Gao, W. C. Wei, J. H. Tan, Y. Wan, Z. Feng, Y. Zhang, Y. Liu, X. Zheng, C. Cao, H. Chen, P. Wang, S. Li, K. T. Wong and C. S. Lee, Anti-Quenching NIR-II J-Aggregates of Benzo[c]thiophene Fluorophore for Highly Efficient Bioimaging and Phototheranostics, *Adv. Mater.*, 2023, **35**, 2211632.

44 M. H. Y. Cheng, K. M. Harmatys, D. M. Charron, J. Chen and G. Zheng, Stable J-Aggregation of an aza-BODIPY-Lipid in a Liposome for Optical Cancer Imaging, *Angew. Chem., Int. Ed.*, 2019, **58**, 13394.

45 Y. Li, T. Ma, H. Jiang, W. Li, D. Tian, J. Zhu and Z. Li, Anionic Cyanine J-Type Aggregate Nanoparticles with Enhanced Photosensitization for Mitochondria-Targeting Tumor Phototherapy, *Angew. Chem., Int. Ed.*, 2022, **61**, e202203093.

46 L. Li, C. Shao, T. Liu, Z. Chao, H. Chen, F. Xiao, H. He, Z. Wei, Y. Zhu, H. Wang, X. Zhang, Y. Wen, B. Yang, F. He and L. Tian, An NIR-II-Emissive Photosensitizer for Hypoxia-Tolerant Photodynamic Theranostics, *Adv. Mater.*, 2020, **32**, 2003471.

47 J. Zou, L. Li, J. Zhu, X. Li, Z. Yang, W. Huang and X. Chen, Singlet Oxygen "Afterglow" Therapy with NIR-II Fluorescent Molecules, *Adv. Mater.*, 2021, **33**, 2103627.

48 J. Liu, X. Zhang, M. Fu, X. Wang, Y. Gao, X. Xu, T. Xiao, Q. Wang and Q. Fan, A diketopyrrolopyrrole-based small molecule with an extended conjugated skeleton and J-aggregation behavior for 808 nm laser triggered phototheranostics, *Biomater. Sci.*, 2023, **11**, 7124–7131.

49 X. Wang, Z. Jiang, Z. Liang, T. Wang, Y. Chen and Z. Liu, Discovery of BODIPY J-aggregates with absorption maxima beyond 1200 nm for biophotonics, *Sci. Adv.*, 2022, **8**, eadd5660.

50 H. M. Pan, C. C. Wu, C. Y. Lin, C. S. Hsu, Y. C. Tsai, P. Chowdhury, C. H. Wang, K. H. Chang, C. H. Yang, M. H. Liu, Y. C. Chen, S. P. Su, Y. Lee, H. K. Chiang, Y. H. Chan and P. T. Chou, Rational Design of Asymmetric Polymethines to Attain NIR(II) Bioimaging at >1100 nm, *J. Am. Chem. Soc.*, 2023, **145**, 516–526.

51 C. C. Wu, E. Y. Li and P. Chou, Reducing the internal reorganization energy *via* symmetry controlled π-electron delocalization, *Chem. Sci.*, 2022, **13**, 7181–7189.

52 P. Xiao, W. Xie, J. Zhang, Q. Wu, Z. Shen, C. Guo, Y. Wu, F. Wang, B. Z. Tang and D. Wang, De Novo Design of Reversibly pH-Switchable NIR-II Aggregation-Induced Emission Luminogens for Efficient Phototheranostics of Patient-Derived Tumor Xenografts, *J. Am. Chem. Soc.*, 2023, **145**, 334–344.

53 H. Lin, Z. Lin, K. Zheng, C. Wang, L. Lin, J. Chen and J. Song, Near-Infrared-II Nanomaterials for Fluorescence Imaging and Photodynamic Therapy, *Adv. Opt. Mater.*, 2021, **9**, 2002177.

54 Y. Gu, H. Lai, Z. Y. Chen, Y. Zhu, Z. Sun, X. Lai, H. Wang, Z. Wei, L. Chen, L. Huang, Y. Zhang, F. He and L. Tian, Chlorination-Mediated π–π Stacking Enhances the Photodynamic Properties of a NIR-II Emitting Photosensitizer with Extended Conjugation, *Angew. Chem., Int. Ed.*, 2023, **62**, e202303476.

55 Y. Zhou, L. Zhu, B. Liu, W. Xu, X. Yang, Y. Liu, B. Ruan, S. Yi, B. Liang, G. Dong and J. Huang, Tailored Zwitterionic Hemicyanine Reporters for Early Diagnosis and Prognostic Assessment of Acute Renal Failure, *Angew. Chem., Int. Ed.*, 2023, **62**, e202315457.

56 Y. Liu, L. Teng, X. F. Lou, X. B. Zhang and G. Song, "Four-In-One" Design of a Hemicyanine-Based Modular Scaffold for High-Contrast Activatable Molecular Afterglow Imaging, *J. Am. Chem. Soc.*, 2023, **145**, 5134–5144.

57 T. B. Ren, W. Xu, W. Zhang, X. X. Zhang, Z. Y. Wang, Z. Xiang, L. Yuan and X. B. Zhang, A General Method To Increase Stokes Shift by Introducing Alternating Vibronic Structures, *J. Am. Chem. Soc.*, 2018, **140**, 7716–7722.

58 A. P. Silva, H. Q. Gunaratne, T. Gunnlaugsson, A. J. Huxley, C. P. McCoy, J. T. Rademacher and T. E. Rice, Signaling Recognition Events with Fluorescent Sensors and Switches, *Chem. Rev.*, 1997, **97**, 1515–1566.

59 R. Lapouyade, W. Czeschka, W. Majenz, W. Rettig, E. Gilabert and C. Rulliere, Photophysics of donor-acceptor substituted stilbenes. A time-resolved fluorescence study using selectively bridged dimethylamino cyano model compounds, *J. Phys. Chem.*, 1992, **96**, 9643.

60 F. Wu, Y. Lu, X. Mu, Z. Chen, S. Liu, X. Zhou, S. Liu and Z. Li, Intriguing H-Aggregates of Heptamethine Cyanine for Imaging-Guided Photothermal Cancer Therapy, *ACS Appl. Mater. Interfaces*, 2020, **12**, 32388–32396.